

Influence of Synthesis Conditions on the Structure of Nickel Nanoparticles and their Reactivity in Selective Asymmetric Hydrogenation

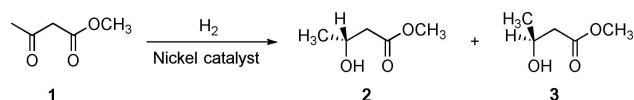
Rosa Arrigo,^{*[a, b]} Simone Gallarati,^[c] Manfred E. Schuster,^[d] Jake M. Seymour,^[e] Diego Gianolio,^[b] Ivan da Silva,^[f] June Callison,^[g, h] Haosheng Feng,^[i] John E. Proctor,^[a] Pilar Ferrer,^[b] Federica Venturini,^[b] David Grinter,^[b] and Georg Held^[b, e]

Unsupported and SiO₂-supported Ni nanoparticles (NPs) were synthesised *via* hot-injection colloidal route using oleylamine (OAm) and trioctylphosphine (TOP) as reducing and protective agents, respectively. By adopting a multi-length scale structural characterization, it was found that by changing equivalents of OAm and TOP not only the size of the nanoparticles is affected but also the Ni electronic structure. The synthesized NPs were modified with (*R,R*)-tartaric acid (TA) and investigated in the asymmetric hydrogenation of methyl acetoacetate to chiral methyl-3-hydroxy butyrate. The comparative analysis of structure and catalytic performance for the synthesized catalysts has

enabled us to identify a Ni metallic active surface, whereby the activity increases with the size of the metallic domains. Conversely, at the high conversion obtained for the unsupported NPs there was no impact of particle size on the selectivity. (*R*)-selectivity was very high only on catalysts containing positively charged Ni species such as over the SiO₂-supported NiO NPs. This work shows that the chiral modification of metallic Ni NPs with TA is insufficient to maintain high selectivity towards the (*R*)-enantiomer at long reaction times and provides guidance for the engineering of long-term stable enantioselective catalysts.

Introduction

The enantioselective asymmetric hydrogenation of unsaturated molecules is broadly applied for the synthesis of pharmaceuticals and fine chemicals, where the biggest challenge is attaining total selectivity to one specific enantiomer.^[1] One of the most studied examples of such reactions is the hydrogenation of β -ketoesters over nickel-based catalysts,^[2] e.g. methyl acetoacetate (MAA) to methyl-3-hydroxybutyrate (MHB), shown in Scheme 1. MHB is an important intermediate in the synthesis of carbonic anhydrase inhibitor MK-0507, used in the



Scheme 1. Hydrogenation of pro-chiral β -ketoester methyl acetoacetate (1) gives two enantiomers, (*R*)- and (*S*)-methyl-3-hydroxybutyrate (2 and 3, respectively). When the surface of the nickel catalyst is modified with (*R,R*)-tartaric acid (also in combination with an inorganic salt such as NaBr), the (*R*)-enantiomer is preferably obtained.

[a] Dr. R. Arrigo, Dr. J. E. Proctor
School of Science
Engineering and Environment
University of Salford
Manchester M5 4WT (UK)
E-mail: r.arrigo@salford.ac.uk

[b] Dr. R. Arrigo, Dr. D. Gianolio, Dr. P. Ferrer, Dr. F. Venturini, Dr. D. Grinter, Prof. G. Held
Diamond Light Source
Harwell Science and Innovation Campus
Didcot OX11 0DE (UK)

[c] S. Gallarati
School of Chemistry
University of St Andrews
North Haugh
St Andrews KY16 9ST (UK)

[d] Dr. M. E. Schuster
Johnson Matthey Technology Centre
Reading RG4 9NH (UK)


[e] J. M. Seymour, Prof. G. Held
Department of Chemistry
University of Reading
Reading RG6 6AD (UK)


[f] Dr. I. da Silva
ISIS Facility
Rutherford Appleton Laboratory
Chilton
Didcot OX11 0QX (UK)

[g] Dr. J. Callison
Department of Chemistry
University College London
London WC1H 0AJ (UK)

[h] Dr. J. Callison
UK Catalysis Hub
Research Complex at Harwell (RCaH)
Rutherford Appleton Laboratory
Harwell Oxon OX11 0FA (UK)

[i] H. Feng
Department of Chemistry
University of Cambridge
Cambridge CB2 1EW (UK)

 Supporting information for this article is available on the WWW under <https://doi.org/10.1002/cctc.201901955>

 © 2019 The Authors. Published by Wiley-VCH Verlag GmbH & Co. KGaA. This is an open access article under the terms of the Creative Commons Attribution License, which permits use, distribution and reproduction in any medium, provided the original work is properly cited.

treatment of glaucoma,^[3] moreover, 3-hydroxyacids are useful building blocks in chiral synthesis.^[4]

This reaction can be carried out with high enantiomeric excess (*ee*) if the surface of the nickel catalyst, e.g. Raney Ni or supported nanoparticles (NPs), is modified with a chiral molecule, typically (*R,R*)-tartaric acid or an amino acid, or by selective poisoning using inorganic salts, such as sodium bromide.^[5] A molecular level understanding of this reaction would be beneficial to tackle the challenge of achieving total selectivity. Particularly, the mechanism by which enantioselectivity is realized at the Ni catalyst surface aided by modifiers is still subject to much debate.^[6–9] Investigations of adsorbate structures of tartaric acid and MAA on model single crystal Ni surfaces have highlighted three possible pathways through which the chiral molecule of the modifier facilitates the formation of the (*R*)-enantiomer: a) through a one-to-one molecular interaction the chiral tartrate molecules adsorbed on the Ni surface control the adsorption geometry of the pro-chiral reagent, which is then reduced on the adjacent exposed metallic Ni surface by chemisorbed H atoms; b) the chiral molecules forming a supramolecular chiral arrangement on the Ni surface desorb from the largely ordered Ni terraces leaving a chiral Ni surface structure responsible for the specific chemisorption of the reagent with the favourable geometry;^[7] c) the interaction of tartrate with oxidised Ni particles facilitates etching of Ni cations from the surface, leaving naturally chiral kink sites on the Ni surface responsible for enantioselectivity.^[9]

Moreover, Keane et al.^[9] found that molecular Ni species leached out during modification manifest enantioselective activity, suggesting that cationic Ni species are also involved in the catalytic reaction.

Despite the large volume of literature available on the adsorption and ordering of chirally pure molecules on single crystals, the complexity of a real catalytic system makes it difficult to unveil the local arrangement of these at their surface. On the other hand, catalytic performances are only available for real catalysts such as supported Ni catalysts^[10] and therefore a direct structure-activity correlation still remains undisclosed. In contrast to single crystals, structurally ill-defined nanoparticles (NPs) enable measurable conversions but suffer from poor enantiomeric selectivity if compared to Raney Ni.^[11] The surface modification proved also in the case of the NPs to influence selectivity and conversion.^[12] Yet, it is unclear whether macroscopically achiral symmetrically round-like NPs with high-index surface sites might create more opportunities for the generation of enantioselective surface ensembles upon chiral modification. Moreover, round-like NPs of different sizes enable a different population of kink sites as well as a different size of the facets, both leading to a different mechanism of action of the TA modifier. An understanding of the impact of NPs size, electronic and crystallographic structure and morphology on the catalytic performance of chirally modified NPs is missing, whilst it can provide important insights for the design of improved enantioselective catalysts. Our aim is to contribute a systematic study of NPs structure-activity correlations, which will enable new mechanistic insights into the catalyst's selective chiral function and the structural transformations responsible

for performance degradation. In this work, we synthesize supported and unsupported nickel nanoparticles of different size and investigate their catalytic performance and physico-chemical properties, such as morphology, size and structure, using synchrotron-based X-ray absorption near edge structure (XANES), extended X-ray absorption fine structure (EXAFS) spectroscopies and X-ray photoelectron spectroscopy (XPS), in combination with bright field scanning transmission electron microscopy (BF-STEM), high angle annular dark field scanning transmission electron microscopy (HAADF-STEM) and X-ray diffraction (XRD).

For a precise control over materials properties at the nanometer level (NPs with narrow size distribution, morphology and composition), we employed the hot-injection colloidal synthesis,^[13] which is based on the reduction of metallorganic or metal salt precursors in high-boiling nonpolar solvents in the presence of surfactant agents.^[14] Rapid injection results in a supersaturated solution where the nucleation of the particles occurs within a short time period. The surfactant molecules capped around the nanocrystals prevent their agglomeration and protect them from possible oxidation upon exposure to atmospheric conditions. Moreover, the surfactant molecules endow the NPs with good colloidal stability.^[15]

We will show that by modifying the synthetic composition, it is possible to tune the NPs' size, as well as the Ni electronic structure. These have significant implications on the resulting reactivity in the investigated reaction.

Results and Discussion

A series of unsupported and SiO₂-supported Ni NPs were synthesized using the hot-injection method to control the size of the NPs by changing the ratio between the reducing (oleylamine, OAm) and protecting (trioctylphosphine, TOP) agents. A sketch of this synthesis is shown in scheme 2.

Table 1 lists the synthetic conditions and samples' notation. The detailed synthetic procedure is reported in the experimental section. Firstly, we will discuss the impact of the composition of the synthesis mixture on the structural features of the resulting unsupported and SiO₂-supported Ni NPs. These will then be correlated with the catalytic performance reported

Table 1. Synthetic conditions and resulting size of Ni NPs.

Samples	OAm ^[b] (x) [eq.]	TOP ^[c] (y) [eq.]	Size ^[d/e] [nm]
Ni_2.5x1.5y	2.5	1.5	1.3/8.0 ± 1.4
Ni_5x1.5y	5	1.5	4.0/7.0 ± 1.3
Ni_10x1.5y	10	1.5	5.6/10.6 ± 1.9
Ni/SiO ₂ _5x1.5y ^[a]	5	1.5	4.7/9.9 ± 1.8
Ni/SiO ₂ _5x0.75y ^[a]	5	0.75	7.3 ^[f] ; 2.5 ^[g] /2.2 ± 0.6
Ni/SiO ₂ _5x3y ^[a]	5	3	3.8/6.5 ± 0.7

[a] 10 wt% loading on CAB-O-SIL 5 M silica, [b] Total number of equivalents of oleylamine (OAm) and 1-octadecene (21) kept constant by varying the amount of solvent, [c] Trioctylphosphine, [d] Determined by XRD, [e] Determined by HAADF-STEM. Average particle size of Ni metal [f] and Ni oxide [g], respectively.

subsequently. To the best of our knowledge, this is the first time that the hot-injection oleylamine–trioctylphosphine Ni NPs synthesis has been used to prepare nanoparticles to be modified with tartaric acid and to catalyse the hydrogenation of methyl acetoacetate.

Traditionally, this synthetic method is performed on a small scale (mmol of nickel precursors, mg of NPs produced) and the NPs are isolated unsupported *via* flocculation procedure, which removes the high-boiling solvent and excess ligands.^[16] We employ the mid-to-high temperature thermal decomposition of Ni(acac)₂ with OAm–TOP as it has been reported to be one of the best strategies for controlling the production of highly monodisperse NPs with narrow size distribution, morphology and composition.^[17] However, as it is preferable to produce larger amounts of catalyst for testing and for multiple spectroscopic and structural characterizations, we attempted to

scale up this well-known synthesis (gram scale) and also support the colloidal NPs on silica for ease of handling.

Structural characterization of unsupported NPs

The low magnification (LM) scanning transmission electron microscopy characterization of the unsupported Ni₅x1.5y catalyst is reported in Figures S1a and b of the supporting information. Accordingly, the NPs appear spherical in shape, or slightly elongated, and have a core-shell structure, where the core is composed of Ni encapsulated in a less than 1 nm thick and rough shell of lower contrast, presumably originating from the capping agents as indicated by XPS and NEXAFS analysis at the C1s and O1s core levels (not shown).

A closer inspection using high resolution high angle annular dark field scanning transmission electron microscopy (HAADF-STEM) (Figure 1a and 1b) enables us to identify detailed structural features for this catalyst. Particularly, Figure 1a shows that the oval NPs is in fact a twinned cuboctahedron with several parallel twin lamellae (as indicated by the arrow) accounting for the anisotropic elongation of the NPs along the C2 axis of the twin. Figure 1b shows more detail of the shell structure, where Ni nanocrystallites are embedded within the organic shell, giving it the roughened aspect seen in the LM STEM images. The Ni₁₀x1.5y sample shows the biggest NPs with more abundantly elongated particles (LM HR STEM in Figures S1c and S1d). The HR-HAADF STEM image in Figure 1c shows a round NP marked by the arrow imaged along the 5-fold axis of a multiply twinned decahedron, composed of 5 face-sharing tetrahedrons. Figure 1d shows an example of twinned NPs composed of face-sharing tetrahedrons and cuboctahedron. Note that in this case, the faces of the octahedron and the tetrahedrons do not match perfectly at the grain boundaries, but an interfacial layer of lower contrast is observed, which is probably due to the residual capping agent (Figure 2f).

A roughened shell of abundant nano-clusters embedded in the organic shell (Figures 1c and 1d) is also seen in this sample. In comparison, the LM STEM images of the Ni_{2.5}x1.5y sample (Figure 2) show mainly round amorphous core-shell NPs where the presence of additional nano-clusters embedded in the

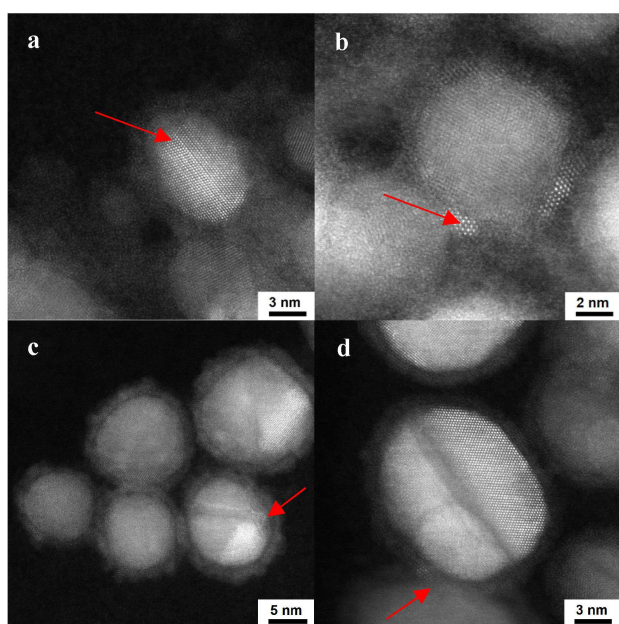


Figure 1. a) and b): HR-HAADF-STEM characterization of Ni₅x1.5y. The arrow indicates the twinned lamellae of the NPs in a) and a smaller Ni NPs embedded in the organic shell in b); c) and d): HR-HAADF-STEM characterization of Ni₁₀x1.5y. In c) the arrow indicates the 5-fold axis of a multiply twinned decahedron. In d) the arrow indicates the Ni atoms of a smaller NPs embedded in the organic shell.

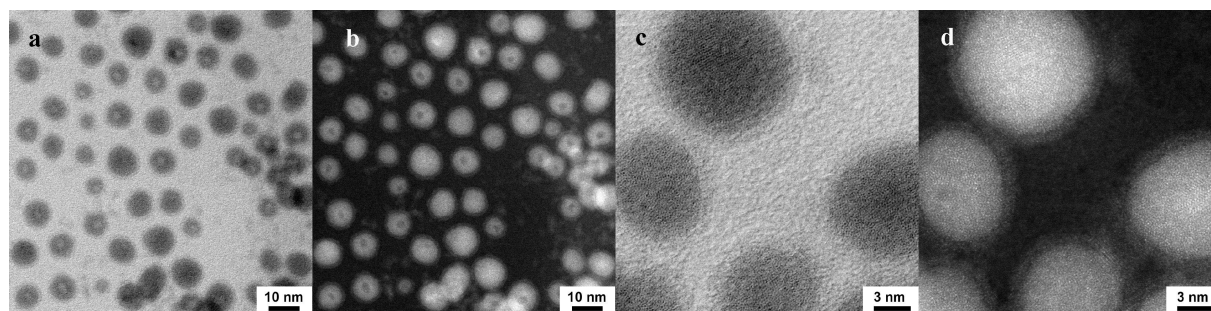


Figure 2. STEM characterization of Ni_{2.5}x1.5y. LM BF-STEM a) and corresponding HAADF-STEM b); HR BF-STEM of a Ni NPs in c) and corresponding HAADF-STEM d).

organic shell is rarely encountered. Peculiarly in this sample, some of the NPs show an inner region of lower contrast, indicating the presence of voids (Figures 2a and b) within the Ni NPs or an area of localized low-density elements such as encapsulated organic matter.

XRD (Figure 3a) confirms the successful formation of metallic Ni nanoparticles without the need of further reduction steps during the synthesis. Particularly, in samples Ni₅x1.5y and Ni₁₀x1.5y, the peaks at 44.4 and 51.7 degrees 2 θ are the characteristic (111) and (200) reflections of metallic nickel, respectively.^[18] In Ni_{2.5}x1.5y, only the most intense (111) reflection is distinguishable, due to peak broadening caused by the smaller crystallite size. Furthermore, no significant contribution from ordered NiO was observed in the XRD patterns of the unsupported NPs.

The average crystallite size determined by STEM for the three samples follows the order of Ni₅x1.5y \leq Ni_{2.5}x1.5y < Ni₁₀x1.5y, as summarized in Table 1. This is in sharp contrast with the size of the coherent crystalline domains determined by XRD. The different trends in average particle size determined by STEM and XRD led us to conclude that significant fractions of the particles are in an amorphous phase and that this is the predominant phase in the Ni_{2.5}x1.5y sample.

The trend in particle size observed for Ni₅x1.5y and Ni₁₀x1.5y is consistent with our expectation upon the systematic variation of the x:y ratio (with x and y being the number of equivalents of OAm and TOP, respectively), as investigated in these experiments. In the colloidal synthesis of nanoparticles, the growth mechanism is generally divided into several stages, occurring at different time frames: nucleation, aggregation growth, and possibly also Ostwald ripening process.^[19] While OAm is expected to control the nucleation rate and growth, TOP acts as capping agent and provides tunable surface stabilization through coordination with the Ni surface, thus hindering the growth. A small OAm:TOP (x:y) ratio during the synthesis leads to small NPs, as in the Ni₅x1.5y catalyst, since the relatively more abundant capping agent TOP further hinders aggregation and growth. Conversely, increasing the x:y ratio leads to larger particles, as in Ni₁₀x1.5y, since the amount of capping agent is relatively decreased, along with its ability to kinetically control the growth step by steric hindrance. Furthermore, by increasing the amount of OAm, the nucleation rate is enhanced, thus larger quantities of nuclei are produced

in solution; such small nuclei are unstable due to the high surface energy and intermolecular forces, leading to growth or rapid aggregation of the nickel nanoparticles^[20] and even formation of twinned structures, as observed in this study. The amount of reducing agent also influences the geometry of the primary nucleus: whilst at a low concentration, the nuclei grow to form small tetrahedrons, which aggregate forming multiply-twinned NPs, with larger amounts of reducing agent the bigger and more thermodynamically favoured cub-octahedrons are formed as well as largely elongated twinned particles (Figures S1c and S1d). Interestingly, when the amount of reducing agent is as low as 2.5 equivalents of Ni(acac)₂ precursor, as in Ni_{2.5}x1.5y, the NPs' formation mechanism is different from the one described above. To understand the formation of amorphous NPs in this condition, one should bear in mind that TOP not only acts as a capping agent to prevent NPs' growth, but also as a source of phosphorous in the synthesis of metal phosphides.^[21] In the case of Ni phosphides, following the initial formation of the Ni metallic core upon Ni precursor decomposition, a subsequent phosphidation step occurs, during which the voids observed are formed through the Kirkendall effect, where outward diffusion of metal atoms from the core is faster than inward diffusion of reactive species.^[22]

HAADF-STEM energy dispersive X-ray (EDX) mapping in Figure 3b confirms the collocation of P and Ni atoms, whereas little signal from O or C is observed, confirming the presence of a predominant Ni phosphide phase, which is amorphous as shown in Figures 2c and 2d.

Raman spectra of the Ni_{2.5}x1.5y sample (Figure S2) exhibited a peak consistent with the most intense mode observed in amorphous NiPS₃ at ca. 600 cm⁻¹,^[23] confirming the existence of Ni–P bonds in this sample. We did not observe the weaker peak at ca. 380 cm⁻¹ seen in amorphous NiPS₃, suggesting that the Ni phosphide in this sample is more amorphous in character than that in the previous work.^[21] We collected 5 spectra from different locations of the sample and all spectra exhibited similar features. Raman spectra of the other samples revealed no evidence for the presence of a Ni phosphide phase. The spin-orbit split Ni2p XPS and NEXAFS characterizations of the as synthesized samples in Figure 4 confirm these findings, whilst providing additional information about the nature of the Ni phosphide phase. We first describe the surface sensitive Ni2p XPS spectrum of the Ni₁₀x1.5y

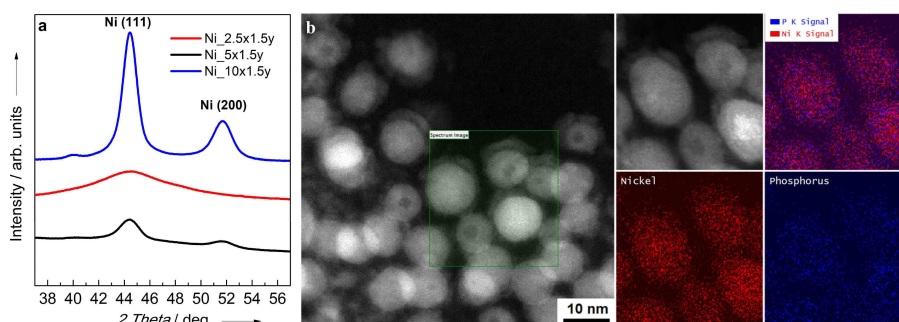


Figure 3. a) XRD characterization; b) HAADF-STEM and EDX elemental mapping for the sample Ni_{2.5}x1.5y.

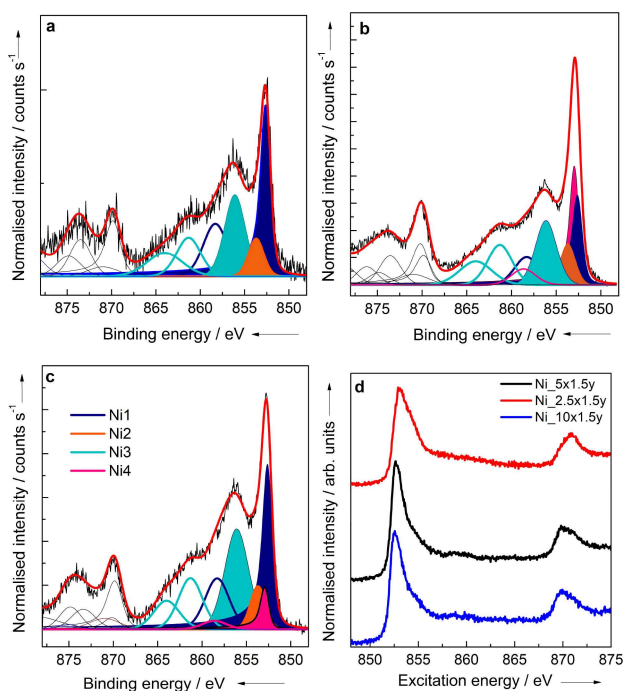


Figure 4. Fitted Ni 2p XP spectra (KE 570 eV) for Ni_{10x1.5y} (a); Ni_{2.5x1.5y} (b) and Ni_{5x1.5y} (c). Fitting: N1 (852.6 eV) is Ni⁰; N2 (852.9 eV) is Ni–P; N3 (853.7 eV) is Ni²⁺ and N4 (856.1 eV) is Ni²⁺/Ni³⁺ in oxide and oxyhydroxide, respectively. Ni L edges NEXAFS spectra for all samples in (d).

sample (Figure 4a). The main metallic Ni 2p_{3/2} peak (Ni1) is found at the binding energy of 852.6 eV, consistently with the literature.^[24] An additional satellite peak attributed to 3d→4s excitation^[24] was found at 5.6 eV above the main line in a reference Ni polycrystalline foil (not shown) and included here in the fitting of the NPs spectra.

A relatively less abundant component Ni2 was found at 853.7 eV, whilst a more abundant component Ni3 was found at 856.1 eV, which is accompanied by two intense satellite peaks at 861.1 eV and 864 eV. Based on literature assignments,^[24–25] the Ni2 component at 853.7 eV is due to Ni^(II) in NiO, whereas the Ni3 component at 856.1 eV is due to a mixed Ni^{(II)/Ni^(III) oxyhydroxide phase. A closer inspection of the spectrum of the Ni_{2.5x1.5y} sample, which is compared to that of Ni_{5x1.5y} in Figure S3, reveals the presence of an additional Ni³⁺ component (Ni4) at 852.95 eV and corresponding low intensity satellite component at 860.5 eV, previously attributed to Ni phosphides.^[26] Note that the same 4 component fitting was applied to all three samples; while only a small contribution of the Ni4 component was needed to afford a good fit of the Ni_{5x1.5y} spectrum (Figure 4c), the fit of the Ni_{10x1.5y} spectrum (Figure 4a) suggests that this component is apparently absent in this case, within the volume probed by these XPS measurements. Since the kinetic energy of the photoelectrons in the present XPS analysis ($h\nu = 1420$ eV, $E_{\text{kin}} = 570$ eV) corresponds to an information depth of approximately 3 nm,^[27] only a fraction of the NPs volume can be characterized. These results are however consistent with the bulk characterization performed by Raman spectroscopy, where only the Ni_{2.5x1.5y}}

sample (Figure S2) shows the vibration breathing mode typical of Ni–P bonds. The analysis of the satellites provides additional information: for Ni_{5x1.5y}, the satellite relative to the metallic component N1 was found with an area of 35% of the main peak, which is consistent with results in the literature,^[26a] moreover, the satellite component relative to the Ni phosphide phase at 860.5 eV in Ni_{2.5x1.5y} is indeed 15% of the main peak, as it was found for a phosphorous enriched Ni₂P phase.^[26a]

Another difference amongst the samples is the ratio between the components contributing to the core of the NPs (Ni1 metallic and Ni4 Ni–P components) and the components relative to the oxyhydroxide layer at the interface with the organic shell (Ni2 and Ni3). Particularly, the higher intensity of the components of the Ni_{2.5x1.5y} core would be an indication of a thinner organic shell, which enables to probe a larger volume of the metallic core. Also, the smaller clusters embedded within the organic shell of Ni_{5x1.5y} and of Ni_{10x1.5y}, which are apparently absent in Ni_{2.5x1.5y}, might be fully detected within the probing depth of these measurements, as opposed to the main NPs' core, which is only partially characterized. This explains the higher abundance of the surface components in Ni_{5x1.5y} and in Ni_{10x1.5y}.^[28] This reasoning is also confirmed by the Ni/C ratio as determined by XPS quantification, which was found to be 2.2, 1.4 and 0.4 for Ni_{2.5x1.5y}, Ni_{5x1.5y} and Ni_{10x1.5y}, respectively.

The spin-orbit split Ni L-edges absorption spectra of these samples in Figure 4d present the L₃ and L₂ resonances maxima of Ni⁽⁰⁾ at 852.6 eV and 870.2 eV, respectively,^[29] whereas in nickel oxide they are reported to be at 853.2 eV (2p_{3/2}3d⁹) and 870.3 eV (2p_{1/2}3d⁹).^[8b,30] However, compared to the spectra reported in literature for Ni metal, the NPs characterized in this study show broadening of the L₃ and L₂ resonances towards higher photon energies. According to Watson and co-workers,^[8b] this broadening is a result of the greater contribution of a surface oxide layer formed under ambient conditions. The most striking difference amongst the spectra reported here is the shift of the main resonance to higher photon energy, by about 0.5 eV, and the significant broadening to the high energy side of the Ni_{2.5x1.5y} sample. Similar results were found for Ni phosphides,^[26a] which is indicative of the partially cationic character of Ni in these compounds, where the higher the P content, the higher the energy shift.

We thus conclude that the reduction of the Ni²⁺ precursor to Ni⁰ by the action of OAm and formation of crystalline Ni NPs occurs below the temperature of the TOP decomposition. Similar conclusions have been reported elsewhere.^[31] However, if the amount of OAm is lower than the quantity needed to reduce quantitatively the Ni²⁺ precursor, as in the case of Ni_{2.5x1.5y}, the molecules of the TOP capping agent will coordinate to the Ni complex in excess in solution. Only when the TOP decomposes at the maximum temperature reached in these experiments (220 °C), the amorphous Ni phosphide particles are formed. The presence of hollow NPs in Ni_{2.5x1.5y} suggests that the Ni phosphide phase can be formed *via* phosphidation of the initially formed Ni⁰ nuclei.^[31]

Structural characterisation of SiO₂-supported Ni NPs

In the case of supported NPs, the NPs were first synthesized and subsequently immobilized onto the silica support. We used 5 equivalents (*x*) of OAm and investigated how changing the amount of protective agent TOP (*y*) influences the nanostructure of the Ni NPs. The same range of OAm:TOP ratios was investigated as in the case of the unsupported NPs. In the subsequent immobilization step, the metal loading was kept low (10%wt) to facilitate the NPs' dispersion on the support. The metal loadings on these samples determined by EDX confirm the quantitative immobilization of the preformed NPs onto the support (Table S1 of the supporting information). While for Ni/SiO₂_5x1.5y and Ni/SiO₂_5x3y the HAADF-STEM images in Figure S4 show the expected nanoparticulate morphology, the Ni/SiO₂_5x0.75y sample shows a cauliflower-like morphology as a result of the low amount of capping agent used, whose role is also to facilitate nuclei agglomeration and sintering.

Due to the SiO₂ component of these materials making the spectroscopic structure analysis by means of electron detection challenging, the electronic structure of the supported samples was investigated by bulk-sensitive XANES and EXAFS at the Ni K-edge in X-ray transmission mode. The samples are compared with a nickel standard (Ni foil) in Figures 5a and 5b, respectively. The XANES spectra exhibit two relevant features: the peak P1 at *ca.* 8336 eV corresponding to either the quadrupole transitions of 1s photoelectrons to Ni3d–O2p hybridized orbitals for the oxide phase or the edge for the metallic phase or a combination of both; the peak P2 at 8352 eV corresponding to transitions of 1s to Ni4p–O2p orbitals^[32] for the oxide phase. With respect to the Ni foil, Ni/SiO₂_5x1.5y and Ni/SiO₂_5x3y clearly show a less intense pre-edge region P1 and a more intense P2 peak. The position of the K-edge (defined as the position of maximum first derivative) was previously found for Ni phosphides between NiO and Ni standards, indicating that the formal oxidation state for phosphides ranges between 0 and 2, where the higher the amount of P, the higher the energy position of the edge.^[33] However, the spectra of these samples (Figure 5a) do not show significant edge-shift as reported for phosphides but rather a systematic increase of the peak P2 intensity and correspondingly a decrease of the P1 resonance. P2 is significantly pronounced in the Ni/SiO₂_5x0.75y spectrum, resembling NiO XANES spectra reported in the literature.^[26,33] Based on this, we propose that the samples are composed of a mixed Ni oxide and metallic phases, whereby spectral variations amongst the samples account for changes in composition of the two phases. Although a P phosphide phase cannot be completely excluded, its contribution should be negligible. The absence of the Ni–P signature in the Raman spectra of the samples (not shown) corroborates this assumption. If we assume that the oxide component is a surface overlayer of the metallic core, the measured increase in the P2 feature corresponds to a higher fraction of NiO and therefore to smaller particles size.^[34]

To prove our assumption, we perform a linear combination fit of the XANES spectra using Ni metal and NiO as standards,

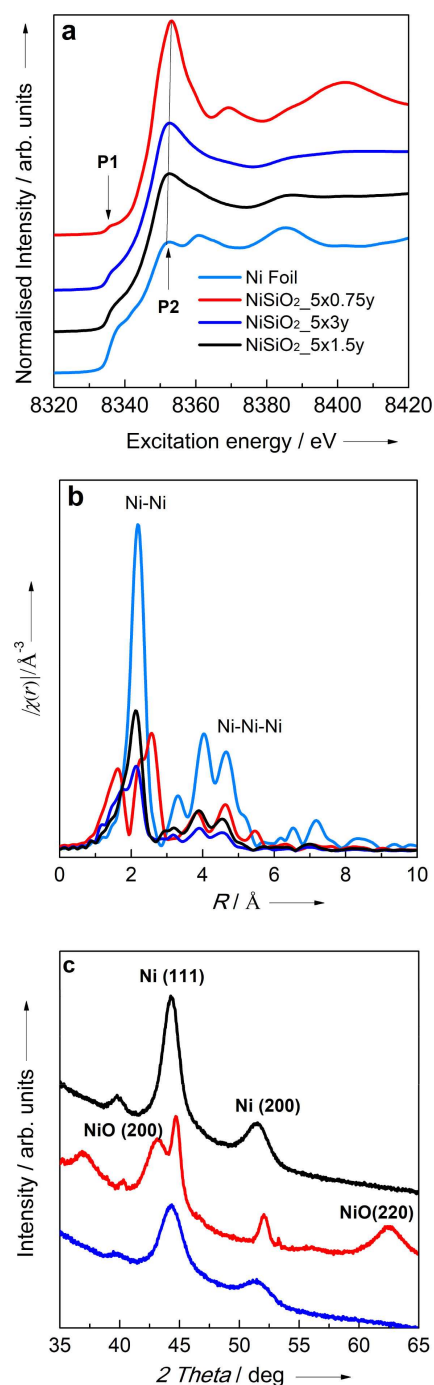


Figure 5. Ni K edge XANES (a) and EXAFS (b) in transmission mode; XRD characterization (c).

which also enabled a quantitative analysis of the two phases, as summarized in Table 2.

The Fourier transforms of the Ni K-edge EXAFS spectra are presented in Figure 5b. The standard nickel foil is also included for comparison. The first peak in face-centered cubic (fcc) Ni is found at 2.48 Å, which is also found in the Ni/SiO₂_5x1.5y and 5x3y samples, although with attenuated intensity, while it is barely visible in 5x0.75y. The peaks at higher distances correspond to main single scattering paths of metallic Ni–Ni

Table 2. XANES Linear Combination Fit and EXAFS fit.

XANES ^[a]	Ni(O)	NiO	R-factor	Red. χ^2
Ni/SiO ₂ _5x1.5y	0.61	0.39	0.005202	0.00063
Ni/SiO ₂ _5x0.75y	0	1.	0.007883	0.001398
Ni/SiO ₂ _5x3y	0.48	0.52	0.006709	0.000847
EXAFS ^[b]	Ni(O)	NiO	R-factor	Red. χ^2
Ni/SiO ₂ _5x1.5y	0.53	0.47	0.032123	3614.764
Ni/SiO ₂ _5x0.75y	0.2	0.8	0.05524	6511.449
Ni/SiO ₂ _5x3y	0.50	0.5	0.030047	1175.56

[a] Linear Combination Fit using Ni metal and NiO as references. [b] EXAFS fit using combination of two models: Ni–Ni scattering paths for metal and Ni–O scattering paths for oxide and a variable ratio between the two.

higher coordination shells (at 3.50, 4.29, 4.96 Å, respectively). In the EXAFS spectra of Ni/SiO₂_5x0.75y, other peaks assigned to single scattering of Ni–O (2.09 Å) and Ni–Ni (2.96 Å) in nickel oxide are clearly visible, indicating that this is the predominant phase in this sample. However, differently from the XANES signals, the EXAFS signals do not respond linearly to the variation in composition of a mixture of phases, but all the signals from different scattering paths interfere depending on their phases. For a quantitative interpretation of the EXAFS data a fit is thus necessary. The results of the fit reported in Table 2 confirm the trend observed for the XANES linear combination fits. Moreover, in the radial distribution function for the Ni/SiO₂_5x3y sample, only the first shell peak is observed, while other samples also show the Ni–Ni higher coordination shell. This means that the Ni/SiO₂_5x3y sample is only short-range ordered. This is also confirmed by the fact that the obtained Debye-Waller factors from the fit is much higher for all shells ($\sigma^2_{1st\ shell} = 0.011$ vs. 0.008, $\sigma^2_{higher\ shells} = 0.0243$ vs. 0.0140).

Furthermore, we note that previous literature on Ni phosphides has indicated that the radial distribution function presents pronounced changes with the content of P and that the FT EXAFS of the Ni/SiO₂_5x3y sample is similar to the spectrum reported for a Ni₁₂P₅ phase with a calculated oxidation state of 0.43.^[33–34] Therefore, it could also be possible that the Ni/SiO₂_5x3y sample might contain a small amount of P as an amorphous phase,^[35] as we would have expected considering that the OAm:TOP ratio used in its synthesis was similar to the one used in the preparation of the unsupported Ni₂5x1.5y sample. However, as discussed above, the Ni phosphide phase can be safely neglected in this data treatment.

X-ray diffraction was used to investigate the structure and phase composition of the samples and to calculate the mean NPs size. Figure 5c compares the XRD patterns of the three supported samples between 35 and 65 degrees 2 θ . Similarly to the unsupported NPs, the Ni/SiO₂_5x1.5y and Ni/SiO₂_5x3y samples show the characteristic peaks at 44.4 and 51.7 degrees 2 θ , which correspond to the nickel (111) and (200) reflections, respectively.^[18] Only the Ni/SiO₂_5x0.75y sample shows a mixture of Ni⁽⁰⁾ and fcc NiO phases (NiO (111), (200) and (220) reflections at 37.0, 43.2 and 62.5 degrees 2 θ , respectively).^[36] Moreover, the diffractograms do not show reflections reported

for crystalline Ni phosphides. Instead, broadening of the main peak indicates a smaller crystallite size.

While trends in the crystallite size calculated from the XRD data for the 5x1.5y (4.7 nm) and 5x3y (3.8 nm) samples are in agreement with what can be imaged by STEM (5x1.5y particles are larger than 5x3y) as summarized in Table 1, the absolute value is very different. Moreover, there is an apparent discrepancy for the Ni/SiO₂_5x0.75y sample. The Ni/SiO₂_5x0.75y sample shows sharp Ni reflections whereby the mean crystallite size was calculated to be 7.3 nm. Whilst these peaks are sharper in the Ni/SiO₂_5x0.75y sample than in the other samples, its main phase is likely to be NiO. The estimated crystallite size for the NiO phase from XRD is around 2.5 nm. However, STEM images clearly show that the catalyst consisted of particles that are much smaller than the other two samples, with an average particle size consistent with the size of the NiO phase as determined by XRD. We therefore propose that for Ni/SiO₂_5x1.5y and Ni/SiO₂_5x3y a large fraction of the NPs is in XRD-amorphous state or twinned NPs with coherent size of the twins as determined by XRD, whereas for Ni/SiO₂_5x0.75y, the large Ni crystallites are covered by smaller oxide NPs forming the cauliflower-like morphology seen in the HAADF-STEM image (Figure S4).

Similarly, to the unsupported NPs, the size and the structural characteristic of the supported nanoparticles can be rationalized taking into account the synthetic conditions and the systematic variation of the x:y ratio. When comparing the Ni/SiO₂_5x3y and Ni/SiO₂_5x1.5y samples, as the number of TOP equivalents (y) is increased, the size of the nanoparticles is reduced, since the growth step is further hindered by relatively more abundant capping agent.^[19,37] We explain the peculiar morphological and structural characteristics of the Ni/SiO₂_5x0.75y sample by taking into account the current opinion in the synthesis of NPs.^[38] Accordingly, in the relative excess of the reducing agent (oleyamine), a large number of metal nuclei are formed; these, assisted by TOP, are prone to growth or agglomeration during the high temperature reaction, forming a small amount of relatively bigger Ni⁰ NPs. However, it is reasonable to assume that at low concentration of TOP ($y < 1$), the nanoparticles being formed in the high temperature reduction of Ni(acac)₂ with OAm are not all being encapsulated by TOP, thus remaining not sufficiently protected from oxidation upon exposure to the environment. The peculiar cauliflower-like morphology of the main oxidic crystallites in the sample also suggests that TOP favours the packing of the small NPs to form bigger twinned NPs.

Catalytic performances of the synthesized unsupported and SiO₂-supported NPs

The synthesized NPs were tested in the enantioselective hydrogenation of MAA. Before the catalytic tests, the NPs catalysts were pretreated with (*R,R*)-TA and NaBr following a modification procedure which proved to be effective in chemisorbing TA on the surface of polycrystalline Ni. The analysis of the surface chemical compositions upon various modification procedures

was afforded by XPS characterization and revealed a very complex chemical speciation which was significantly affected by the experimental conditions. It is thus expected that the surface chemical composition of the reactive interface of the catalyst changes dynamically under hydrogenation conditions. A more detailed discussion is reported in the supporting information (Figure S5). The combined NaBr and TA modification was also confirmed to enhance the enantiomeric selectivity towards (*R*)-MHB as well as the activity in the case of Raney Nickel (Table S2) as reported in the literature.^[1,13]

The chirally modified NPs produce both (*R*)-MHB and (*S*)-RHB (Figure 6). No other product was observed under the experimental conditions used.

Table 3 summarizes the catalytic performance of the supported and unsupported nanoparticles in the hydrogenation of MAA. The final enantiomeric excess (*ee*) is calculated according to Equation (1), given the concentration of (*R*)-MHB and (*S*)-MHB at the end of the reaction; where possible, the instantaneous selectivity towards (*R*)-MHB is compared at the same value (50%) of total MAA conversion, thus the values reported here are extrapolations from the fits presented in Figure 6.

As it can be seen from Table 3, the activity (total MAA conversion) of the unsupported Ni_{5x1.5y} and Ni_{10x1.5y} samples at 22 h of reaction did not vary significantly, indicating that there is no size-effect on the activity at this reaction time and at such variations of the crystalline domains (4.0 nm vs. 5.6 nm from XRD); in contrast, the activity of the Ni_{2.5x1.5y} was significantly inferior (36% tot. conv.). Note that the as prepared sample is composed of large particles of average diameter of 8 nm composed of a predominantly amorphous Ni phosphide phase, whereas the size of metallic crystallites is much smaller (*ca.* 1.3 nm in Table 1).

Figures 6a and 6b report the instantaneous conversion of MAA and selectivity as a function of the reaction time for the unsupported and SiO₂-supported NPs, respectively. The total conversion of MAA as a function of reaction time is reported in Figure 6c. With respect to the total conversion and selectivity, the instantaneous conversion and selectivity provide a direct evaluation of the changes in the catalytic performances as well as deactivation. Indeed, we can observe that the activities of the catalysts are steadily increasing for the unsupported Ni NPs. This is an indication that the chemisorbed species composing the surface overlayer detach from the Ni surface with time and as a consequence new surface is exposed during the reaction, which is available for catalysis.

However, the increase in activity is not reflected in an increase of the selectivity towards (*R*)-MHB. Particularly, for the unsupported Ni_{5x1.5y} and Ni_{10x1.5y} samples, the selectivity towards (*R*)-MHB is maintained constant within the time frame investigated, regardless of the MAA conversion achieved.

Interestingly, we observe for the unsupported Ni_{2.5x1.5y} sample that at the beginning of the reaction the selectivity towards (*R*)-MHB is higher but decreases very rapidly to reach the value of *ca.* -3% *ee*. This value seems to be characteristic for these unsupported NPs systems, in conditions which the chiral modification is no longer present.

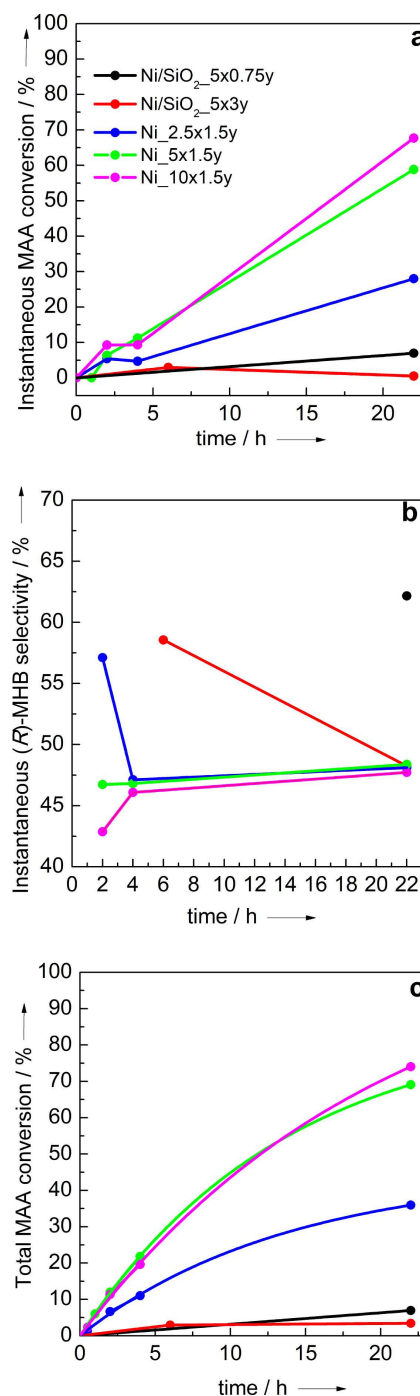


Figure 6. Instantaneous conversion of MAA vs. time of reaction (a) and corresponding selectivity to (*R*)-MHB (b). Total conversion of MAA (c).

In general, the measured activities for the SiO₂-supported Ni NPs samples were very poor with a very low conversion, in part due to the low loading of Ni (10% in weight) in these catalysts. However, at such a low conversion, the Ni/SiO₂_5x0.75y sample shows an *ee* of 24%, which is the highest *ee* towards (*R*)-MHB observed in this study and similar to the one obtained for Raney Ni modified using the same procedure (Table S2).

Samples	Tot. MAA conv. [%] ^[b]	Inst. (<i>R</i>)-MHB selec. [%] ^[c]	Final <i>ee</i> [%] ^[d]
Ni_5x1.5y	69	48	-3
Ni_2.5x1.5y	36	48 ^[e]	-3
Ni_10x1.5y	74	46	-4
Ni/SiO ₂ _5x0.75y	7	62 ^[f]	24
Ni/SiO ₂ _5x3y	3	48 ^[g]	7

[a] Reaction conditions: 0.5 g of unsupported NPs or 1 g of Ni/SiO₂, MAA (0.15 mol), MeOH solvent (15 mL), H₂ 20 bar, T 60 °C. [b] Conversion after 22 h of reaction. [c] Unless otherwise stated, selectivity at the same value (50%) of total MAA conversion. [d] Positive values indicate (*R*)-selectivity, negative (*S*)-selectivity. [e] Value at 36% conversion. [f] Value at 7% conversion. [g] Value at 3% conversion.

Similarly, the selectivity of Ni/SiO₂_5x3y towards (*R*)-MHB is initially high but decreases with time.

Figure 7 shows BF-STEM and HAADF-STEM images of Ni_2.5x1.5y after the reaction. LM images of the same sample are reported in Figure S5. It is worth noting that, despite the core-shell structure still being present, the core of the NPs is now clearly crystalline whereas the shell is much thicker. Interestingly, the shell is now composed of more abundant crystalline nano-clusters covering the overall surface and imparting a much rougher aspect to the surface shell structure (Figure 7). This clearly indicates that Ni NPs, which are initially in the Ni-P amorphous phase, undergo structural changes towards the formation of a more crystalline Ni over-layer during the hydrogenation reaction.

Raman spectra of Ni_2.5x1.5y after 22 h of reaction suggest that the sample is highly inhomogeneous in character (Figure S6). The five spectra taken at different spots were quite different, with two exhibiting a weak peak at *ca.* 600 cm⁻¹, suggesting that a small amount of Ni phosphide phase may now only be present in certain regions of the sample. However, the structural characteristics seen in Figure 7 are not enabling enantiomeric differentiation.

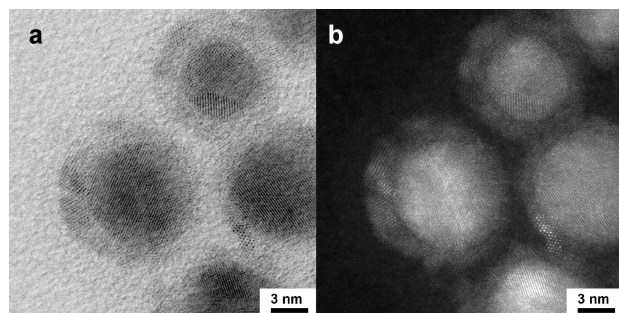


Figure 7. BF-STEM images (a) and corresponding HAADF-STEM (b) of Ni_2.5x1.5y after 22 h of hydrogenation reaction.

Correlation between catalytic performances and structural characterization

The comparative analysis of the reactivity data of the unsupported samples shows that large metal crystallites lead to higher conversion. In contrast, enantioselectivity is mainly unaffected by the size of the NPs. A higher initial value of selectivity towards the (*R*)-enantiomer was obtained on the Ni_2.5x1.5y catalyst, which contains cationic Ni species in the form of a phosphide. However, the selectivity for (*R*)-MHB reached a similar value for all unsupported catalysts after 22 h of reaction.

The measured activities for the supported samples were generally very poor (Figure 7b). This is only in minimal part due to the low loading of Ni (10% in weight) in these catalysts. Indeed, the Ni/SiO₂_5x0.75y sample, which was initially present predominantly as a NiO phase, shows a particularly low conversion of 7% after 22 h of reaction, probably due to the slow reduction to form the active hydrogenation Ni⁰ phase. Interestingly, in this condition, the catalyst shows the highest *ee* towards (*R*)-MHB observed in this study (24%).

Indeed, in this study we could identify that high selectivity towards (*R*)-MHB is obtained when a cationic Ni phase is present (NiO for the supported or NiP for the unsupported catalysts).

It is generally observed that (*R*)-MHB is favoured when (*R,R*)-tartaric acid is used as modifier together with NaBr and was confirmed in this work also for Raney Nickel investigated under the same reaction conditions (Table S2).

The observation of enantioselective differentiation for some of the catalysts at the beginning of the reaction further confirms that during the *ex situ* modification step with (*R,R*)-tartaric acid and NaBr, some level of exchange of the capping agents with the chiral modifier takes place as also proved by the XPS in Figure S5 for polycrystalline Ni. However, the fact that the instantaneous conversion increases steadily with time whereas the selectivity at higher conversion is maintained at the value of the racemic composition indicates that the capping agent was not quantitatively substituted by TA and NaBr.

In fact, as the achiral capping agent detaches from the round shaped NPs, the amount of left and right kink sites or left and right planes is equal and thus a macroscopically achiral metal surface is freed.^[1] At this point, the selectivity reaches the value which is characteristic of an unmodified Ni⁰ surface.

Moreover, we suggest that the lack of enantiomeric differentiation of the Ni_5x1.5y and Ni_10x1.5y samples is the result of the weak chemisorption of the chiral molecules on the Ni metallic surface, which desorb easily from the Ni surface upon hydrogenation conditions, where the dynamic surface diffusion of metal atoms and restructuring typical for NPs^[28] results in an inefficient chiral modification. The weak chemisorption of TA on metallic Ni was also proved for the case of polycrystalline Ni reported in the supporting information (Figure S5).

Thus, from the catalytic data presented here, it may be assumed that the mechanism that involves the formation of a chiral arrangement of TA molecules on flat Ni surfaces, leaving a chiral imprint on it upon TA desorption,^[39] is the least probable mechanism to explain the chiral action of TA and

NaBr in these nanoparticulate systems. The higher enantiomeric selectivity at low reaction times on oxidized samples can be correlated to the higher chelating affinity of the carboxylate species of TA–Na towards cationic Ni. As discussed in previous literature,^[9–10] TA is highly corrosive and Ni²⁺ species coordinated to TA can leach out leaving (*R*)-kinks behind. However, whilst we cannot rule this mechanism out, we would have expected that the rapid dynamic restructuring of these (*R*)-kink sites would not allow us to be able to measure such a transient and short-lived enantiomeric differentiation similarly to the case of the metallic NPs Ni₅x1.5y and Ni₁₀x1.5y. We therefore suggest that the most probable mechanism that describes our results involves strongly chemisorbed TA on the surface of oxidized Ni. Indeed, TA binds more strongly on NiO than on Ni metal, and under hydrogenation conditions prevents its reduction. However, on adjacent unprotected reduced Ni⁰, the active phase for the hydrogenation, TA can assist the favourable chemisorption of MAA to form (*R*)-MHB. This is consistent with previous work on the adsorption of tartaric acid and MAA on Ni surfaces.^[7] Particularly, a hydrogen bonding interaction between the hydroxyl of a TA molecule chemisorbed *via* the two carboxylates on Ni^[7] and the ester–oxygen of a MAA molecule chemisorbed *via* the ester–carbonyl might occur. This intermolecular interaction of the chemisorbed species constrains the interaction of MAA through the ketone carbonyl with the chemisorbed H atoms on the Ni from the side that leads to the (*R*)-enantiomer formation. However, with time, the NPs are reduced under hydrogenation and, simultaneously, TA detaches more easily from the surfaces of the NPs leaving achiral NPs.

Conclusions

In this work, we have synthesized Ni NPs and SiO₂-supported Ni NPs obtained *via* hot-injection using different ratios of reducing and capping agents and characterized the morphology, nanostructure and chemical composition. Size and phase control during synthesis was revealed together with the impact of these characteristics on the resulting catalytic performance in the selective enantiomeric hydrogenation of MAA. Our findings imply that the more likely role played by the modifier under the conditions investigated is not to generate the chiral Ni surface, but rather to be involved in a chemical interaction with the prochiral substrate, thus assisting a specific configuration of chemisorption of the latter on the metallic Ni active surface that leads to the selective (*R*)-enantiomer formation.

It is therefore evident that to design highly active and (*R*)-selective hydrogenation catalysts, a combination of large Ni metallic surface domains is needed, together with the existence of Ni cationic islands where the chiral modifier can strongly chemisorb to assist the side-by-side selective hydrogenation of MAA. We speculate that, at an optimal concentration, sodium bromide plays a similar role, whereas an excessive amount could act as irreversible poison of the catalyst surface.

Experimental Section

Materials and Methods

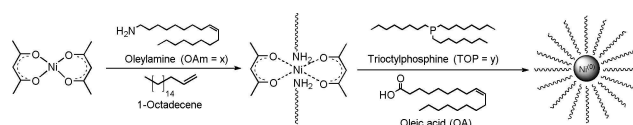
The synthesis of both unsupported and silica-supported nickel nanoparticles *via* thermal decomposition reduction method was adapted from the literature.^[20b] Oleylamine (OAm, *x*) was used as reducing agent whereas trioctylphosphine (TOP, *y*) and oleic acid were used as capping agents (Scheme 2).

The amount of oleylamine or TOP was varied as a strategy to tailor the particle size, as described in Table 1. The total number of equivalents of OAm and solvent (1-octadecene) was kept constant (21 molarequivalents), therefore the volume of solvent was also systematically varied. All other parameters (concentration of nickel precursor, temperature, and oleic acid, reaction time) were not varied. Reaction yields (mass of isolated NPs with respect to number of moles of Ni precursor) were typically between 70% and 80%.

List of reagents: Technical grade nickel(II) acetylacetonate (95%), oleylamine (70%), trioctylphosphine (90%) and 1-octadecene (90%) reagents were purchased from Sigma-Aldrich and used as received without further purification. Oleic acid (≥99%, GC grade), L-(+)-tartaric acid (ACS reagent, ≥99.5%), anhydrous sodium bromide (ACS reagent, ≥99%) and methyl acetoacetate (Reagent-Plus®, 99%) were also purchased from Sigma-Aldrich and used as received. CAB-O-SIL® (M-5 scintillation grade, 200 m²/g) was purchased from Acros Organics (Fisher Scientific) and used as received. Polycrystalline nickel discs (10×1.5 mm) were sourced from Goodfellow Cambridge. Raney Ni was purchased from Sigma-Aldrich.

Unsupported NPs – variation of *x* (OAm) number of equivalents

Reactions were carried out under an atmosphere of high-purity argon to protect nickel and trioctylphosphine from oxidation; the temperature was controlled with a thermocouple placed directly inside the reaction vessel. In a typical synthesis, Ni(acac)₂ (3.46 g, 13.45 mmol) and oleylamine (22.13 mL, 67.27 mmol) were mixed together in 68.87 mL of 1-octadecene and stirred magnetically at 65–70 °C in a flow of Ar under reflux conditions. Once the mixture was completely dissolved, trioctylphosphine (9 mL, 20.18 mmol), after having been degassed with nitrogen for 10 minutes, was rapidly injected into the flask, followed by re-setting the temperature to 120 °C and holding it for 10 minutes. The mixture was then rapidly heated to 220 °C over the course of 15 minutes for nucleation and ripening of the nanoparticles. After 2 hours of reflux, the synthesis was halted and the flask cooled to room temperature. Oleic acid (1.35 mL, 4.25 mmol) was then added to the mixture, followed by ultra-sonication for 10 minutes. The nickel nanoparticles were then precipitated by adding anhydrous ethanol (150 mL) and centrifuging the dispersion at 8500 rpm for 30 min. The wet catalyst was then suspended in a mixture of hexane (10 mL) and anhydrous ethanol (30 mL) and centrifuged for a further 30 min at 8500 rpm. This process was repeated twice.



Scheme 2. Hot injection synthesis of monodisperse NPs. Adapted from ref. [15b].

Supported nanoparticles – variation of γ (TOP) number of equivalents

In the case of supported catalysts, the protocol above was followed but, instead of precipitating the NPs *via* treatment with a poor/good solvent mixture (ethanol/hexane) and centrifugation (flocculation method), they were supported on silica (CAB-O-SIL 5M). Amounts of Ni(acac)₂ precursor, OAm, TOP, 1-octadecene and SiO₂ support were adjusted to obtain ca. 4 g of sample with a theoretical NPs loading of 10 wt% (assuming 100% reduction yield and 100% incorporation of nanoparticles on the support). To achieve the impregnation of the nanoparticles on silica, CAB-OSIL 5 M was first dispersed in absolute ethanol (150 mL); under vigorous stirring, the reaction mixture was added to the support dispersion, which was then filtered under suction and washed multiple times with copious EtOH until the runnings were essentially colourless, indicating removal of excess surfactant.

Ex situ modification with tartaric acid

All nanoparticulate systems and the Raney Nickel catalysts were subjected to *ex situ* modification with (*R,R*)-tartaric acid (TA). The catalyst (0.5 g of unsupported NPs, 1 g of Ni/SiO₂ sample) was refluxed at 100 °C for 1 h in 100 mL of the modification solution (1 wt% TA, 20 wt% NaBr co-modifier, pH 5.1 adjusted with 1 M NaOH), followed by washing with one portion of water (50 mL) and 2 × 25 mL portions of methanol. Prior to modification, the supported nanoparticles were treated under a stream of 10% hydrogen gas in He gas at 300 °C for 1 h. The samples were then cooled to r.t. under N₂ before the modification solution was injected into the vessel, thus avoiding exposure to air.

Other samples were obtained starting from Raney Ni, which was modified in an aqueous solution containing either only 20 wt% NaBr or 1 wt% TA, following the same procedure as indicated above.

Ex situ modifications of polycrystalline Ni for XPS analysis

The polycrystalline Ni discs were first reduced under a constant steam of 5% H₂ in He in a tube furnace at 450 °C for 16 h before being stored under Millipore water for transport to minimise contact with atmospheric O₂. Following, the discs were subjected to chemical modifications using a Schlenk line. 2 discs were transferred into each modifying solution; (1) 150 mL of Millipore H₂O for the unmodified sample; (2) 1.5 g of TA in 150 mL of Millipore H₂O; (3) 30 g of NaBr in 150 mL of Millipore H₂O; (4) 1.5 g of TA and 30 g of NaBr in 150 mL of Millipore H₂O. Millipore water used in these experiments was either degassed under vacuum prior to being used (1 and 2) or boiled under N₂ for 30 min before being used (3 and 4). Solution 1 containing the discs was not refluxed, while solutions 2–4 were refluxed under N₂ for 1 h.

After refluxing, a disc was removed from solutions 2–4 and rinsed with Millipore water and stored under N₂ degassed water for at least 60 h. The samples were then mounted on sample holders under water before being placed in the load lock to pump away the water. X-ray photoelectron spectroscopy (XPS) spectra were then taken of the Ni 2p, O 1s, C 1s and Valence Band regions.

Catalyst characterisation

The supported and unsupported NPs were characterized prior to exposure to H₂ and *ex situ* modification with tartaric acid.

X-ray powder diffraction measurements were carried out on a Rigaku Miniflex 600 diffractometer, using CuK α radiation. A silicon NIST SRM 640e standard sample was firstly measured, in order to obtain the instrumental resolution function of the diffractometer. The obtained diffraction pattern for each sample was Rietveld refined using TOPAS 5 software^[40] and the corresponding crystallite sizes were estimated by using calculated integral breadth-based volume-weighted column heights^[41] assuming monodisperse spherical systems of particles.

X-ray absorption fine structure spectra at the Ni K-edge were obtained from experiments at the B18 beamline in Diamond Light Source, UK.^[42] The measurements were carried out using a fixed-exit double-crystal Si(111) monochromator and the Pt-coated branch of collimating and focusing mirrors. Harmonic rejection mirrors were placed in the beam path and used as a low-pass filter to remove higher energy harmonics. The beam size at the sample position was approximately 1 × 1 mm. All samples were prepared in forms of pellets (13 mm diameter) mixing 50 mg of sample with 50 mg of cellulose to optimize the edge jump and total transmission. The measurement was performed at room temperature in transmission mode using 3 ion chambers filled with following gases: 300 mbar N₂ + 700 mbar He (I0); 150 mbar Ar + 850 mbar He (I1, I2). The spectra were collected in quick EXAFS mode by continuously scanning the monochromator with a constant energy step size of 0.3 eV. The scan covered an energy range from 8133.15 to 9333 eV, corresponding to a k -range of 16 Å⁻¹. For each sample, 3 scans were acquired and subsequently merged to improve the signal to noise ratio. Data were normalised using the program Athena^[43] with a linear pre-edge and 2nd order polynomial post-edge. After background subtraction, the resulting $\chi(k)$ functions were k^2 -weighted and Fourier transformed in a range from 2 to 15.5 Å⁻¹. The EXAFS fit was performed using the two references structures, Ni⁰ and NiO, for which the most relevant single and multiple scattering paths were calculated. The amplitude of each signal was then described as a function of the ratio of the phases generating the scattering path and the ratios optimized during the fit of the experimental data.

X-ray photoelectron spectroscopy (XPS) and near edge X-ray absorption fine structure (NEXAFS) measurements in the soft X-ray regime were carried out at the VERSOX end station and beamline at the UK synchrotron facility Diamond Light Source. The freshly prepared samples from atmospheric environment were deposited on a Si wafer and directly exposed to vacuum (10⁻⁸ mbar) in the XPS chamber. XPS measurements were performed by applying a suitable excitation energy corresponding to a kinetic energy (KE) of the photo-emitted electrons of 450 eV for the core levels Ni2p, C1s and O1s. The energy pass Ep was normally set to 20 eV. The core levels envelopes were fitted using Casa XPS software after subtraction of a U2 Tougaard background.

The fittings of the Ni2p spectra were performed by considering four core-level components. A DS function line-shape was used for both the metallic Ni1 and phosphide Ni4 components whereas two components with a Gaussian-Lorentzian (GL) line-shape (Ni2 and Ni3) were included accounting for Ni²⁺ and Ni²⁺/Ni³⁺ oxyhydroxide components, respectively. The fitting of the spectra was done by constraining the peak position by ±0.05 eV. The peak area ratio between the Ni2p_{3/2} and Ni2p_{1/2} spin orbit split transitions was constrained approximately to the theoretical value of 2:1 and the distance between the two-spin orbit split transition was 17.2 eV. Binding energies (BEs) were referenced to the maximum of the C1s core level peak (284.3 eV) measured after every other core level measurement at the corresponding excitation energy. The satellite feature for Ni⁰ is 5.7 eV upshift with respect to the core level, whereas its intensity is 35% of the main peak.

Auger Electron Yield (AEY) NEXAFS spectra were recorded with an analyser setting of 50 eV pass energy (E_p) and electron kinetic energy (KE) of 700 eV, 520 eV and 240 eV for Ni L, OK and CK edges, respectively. The beam-line setting was $0.5 \mu\text{m} \times 0.04 \mu\text{m}$ exit slit (ES) and fix focus constant (cff) 2.0.

Bright field (BF) and high angle annular dark field scanning transmission electron microscopy (HAADF STEM) images were acquired on a probe corrected ARM200F at the ePSIC facility (Diamond Light Source) equipped with a cold-FEG and operated at an acceleration voltage of 200 keV enabling a resolution of 0.78 Å. Measurement conditions were a CL aperture of 30 μm , convergence semiangle of 24.3 mrad, beam current of 12 pA, and scattering angles of 0–10 and 35–110 mrad for BF and HAADF STEM respectively. Samples were deposited onto 3 mm holey carbon Cu-grids for TEM analysis.

Raman spectroscopy experiments were performed using 532 nm laser excitation and a conventional single grating (1200 lines per mm) 0.32 m Raman spectrometer. The spectra were calibrated using the intense phonon mode in Si at 520.0 cm^{-1} , and the spectral resolution was verified to be at worst 3.2 cm^{-1} half width half maximum. The notch filters on the spectrometer allowed collection of data down to 270 cm^{-1} . This was verified by the observation of a radial breathing mode peak from a single-walled carbon nanotube sample centered on this wavenumber.

Hydrogenation reaction of MAA under batch conditions

The modified Ni catalysts were then tested for the hydrogenation reaction of methyl acetoacetate (17.0 g, 0.15 mol) in methanol (15 mL) using a batch reactor at a working H_2 pressure of 20 bar, temperature of 60°C , with stirring set to 750 rpm. 0.5 g of unsupported NPs and 1 g of supported NPs were used for the catalytic tests. Samples of the solution were taken over a period of 22 h, filtered to remove any solid catalyst and prepared for GC analysis (500 μL mixed with 10 μL of decane). Shimadzu GC 2014 with FID and Shimadzu AOC-20i autosampler attachment were used for experimental analysis, in combination with a Supelco Analytical Beta Dex 325 capillary column. From the chromatographs, the concentration of each species x was calculated from the concentration of the internal standard (IS, decane), the detector response factor (DRF) of each analyte x , and the peak area of analyte and IS (A_x and A_{IS}), as shown in Equation (2). Catalytic data were then calculated from the concentrations of MAA, (S)-MHB and (R)-MHB. The instantaneous conversion of MAA and the instantaneous selectivity towards the (R)-enantiomer with respect to the products were calculated as given in Equations (3) and (4). Exponential and linear Equations were used to fit the conversion and selectivity data, respectively. Equation (5) was used to calculate the total conversion of MAA and an exponential function was used to fit the data (Figure S4).

$$ee (\%) = \frac{[(R) - \text{MHB}] - [(S) - \text{MHB}]}{[(R) - \text{MHB}] + [(S) - \text{MHB}]} \times 100 \quad (1)$$

$$[x] = \left(\frac{A_x}{A_{\text{IS}}} \right) \times \left(\frac{[\text{IS}]}{\text{DRF}} \right) \quad (2)$$

$$\text{Inst. MAA conv. } (\%) = \frac{([\text{MAA}]_{t-1} - [\text{MAA}]_t)}{[\text{MAA}]_{t-1}} \times 100 \quad (3)$$

$$\text{Inst. (R)-MHB selectivity (with respect to products) } (\%) = \frac{([\text{R} - \text{MHB}]_t - [\text{R} - \text{MHB}]_{t-1})}{\left[\left(\frac{[\text{R} - \text{MHB}]_t - [\text{R} - \text{MHB}]_{t-1}}{[\text{R} - \text{MHB}]_{t-1}} \right) + \left(\frac{[\text{S} - \text{MHB}]_t - [\text{S} - \text{MHB}]_{t-1}}{[\text{S} - \text{MHB}]_{t-1}} \right) \right]} \times 100 \quad (4)$$

$$\text{Total MAA conv. } (\%) = \frac{([\text{MAA}]_0 - [\text{MAA}]_t)}{[\text{MAA}]_0} \times 100 \quad (5)$$

Acknowledgements

SG acknowledges the Year in Industry placement scheme at Diamond Light Source (2017–18, “Chirally modified catalyst nanoparticles” project on the VERSOX beamline in collaboration with the UK Catalysis Hub) and the External Placement scheme of the School of Chemistry in the University of St Andrews. HF is grateful for the summer student placement program at Diamond Light Source. The authors would like to thank Matteo Aramini (DLS) for helping with the preparation of the TOC and Yaroslav Odarchenko (UCL and RCaH) for preliminary AFM measurements on the unsupported NPs. The UK Catalysis Hub is kindly thanked for resources and support provided via our membership of the UK Catalysis Hub Consortium and funded by EPSRC (portfolio grants EP/K014706/1, EP/K014668/1, EP/K014854/1, EP/K014714/1 and EP/I019693/1).

Keywords: Nanoparticles · Ni phosphides · Hot-injection · enantioselective hydrogenation · XPS · XAFS · HRTEM

- [1] a) T. Mallat, E. Orglmeister, A. Baiker, *Chem. Rev.* **2007**, *107*, 4863–4890; b) G. Kyriakou, S. K. Beaumont, R. M. Lambert, *Langmuir* **2011**, *27*, 9687–9695; c) F. Meemken, A. Baiker, *Chem. Rev.* **2017**, *117*, 11522–11569.
- [2] Y. Izumi, in *Advances in Catalysis*, Vol. 32 (Eds.: D. D. Eley, H. Pines, P. B. Weisz), Academic Press, **1983**, pp. 215–271.
- [3] T. J. Blacklock, P. Sohar, J. W. Butcher, T. Lamanec, E. J. J. Grabowski, *J. Org. Chem.* **1993**, *58*, 1672–1679.
- [4] a) C. H. Martin, H. Dhamankar, H.-C. Tseng, M. J. Sheppard, C. R. Reisch, K. L. J. Prather, *Nat. Commun.* **2013**, *4*, 1414; b) B. Hu, M. Prashad, D. Har, K. Prasad, O. Repič, T. J. Blacklock, *Org. Process Res. Dev.* **2007**, *11*, 90–93; c) H. S. Lee, D. H. Kim, *Biorg. Med. Chem.* **2003**, *11*, 4685–4691; d) D. Zhang, M. A. Hillmyer, W. B. Tolman, *Macromolecules* **2004**, *37*, 8198–8200.
- [5] a) M. A. Keane, *Langmuir* **1997**, *13*, 41–50; b) C. J. Baddeley, *Top. Catal.* **2003**, *25*, 17–28; c) C. J. Baddeley, T. E. Jones, A. G. Trant, K. E. Wilson, *Top. Catal.* **2011**, *54*, 1348–1356.
- [6] a) P. Tsaousis, J. Ontaneda, L. Bignardi, R. A. Bennett, R. Grau-Crespo, G. Held, *J. Phys. Chem. C* **2018**, *122*, 6186–6194; b) R. E. J. Nicklin, A. Shavorskiy, F. A. Akgul, Z. Liu, R. A. Bennett, M. Sacchi, G. Held, *J. Phys. Chem. C* **2018**, *122*, 7720–7730.
- [7] T. E. Jones, C. J. Baddeley, *J. Mol. Catal. A-Chem.* **2004**, *216*, 223–231.
- [8] a) J. Ontaneda, R. E. J. Nicklin, A. Cornish, A. Roldan, R. Grau-Crespo, G. Held, *J. Phys. Chem. C* **2016**, *120*, 27490–27499; b) D. J. Watson, S. Acharya, R. E. J. Nicklin, G. Held, *Surf. Sci.* **2014**, *629*, 108–113.
- [9] M. A. Keane, G. Webb, *Chem. Commun.* **1991**, 1619–1621.
- [10] M. A. Lopez Martinez, PhD Thesis, https://etheses.bham.ac.uk/id/eprint/1491/2/Lopez_11_PhD.pdf
- [11] T. Osawa, Y. Amaya, T. Harada, O. Takayasu, *J. Mol. Catal. A* **2004**, *211*, 93–96.
- [12] a) M. A. Keane, *Can. J. Chem.* **1994**, *72*, 372–381; b) M. A. Keane, *Catal. Lett.* **1993**, *19*, 197–209.
- [13] a) S. G. Kwon, T. Hyeon, *Small* **2011**, *7*, 2685–2702; b) S. Mourdikoudis, L. M. Liz-Marzán, *Chem. Mater.* **2013**, *25*, 1465–1476.

- [14] a) C. B. Murray, S. Sun, W. Gaschler, H. Doyle, T. A. Betley, C. R. Kagan, *IBM J. Res. Dev.* **2001**, *45*, 47–56; b) C. B. Murray, S. Sun, H. Doyle, T. Betley, *MRS Bull.* **2001**, *26*, 985–991.
- [15] a) S. Campisi, M. Schiavoni, E. C. Chan-Thaw, A. Villa, *Catalysts* **2016**, *6*; b) J. V. I. Timonen, E. T. Seppälä, O. Ikkala, R. H. A. Ras, *Angew. Chem. Int. Ed. Engl.* **2011**, *50*, 2080–2084; c) E. V. Shevchenko, D. V. Talapin, H. Schnablegger, A. Kornowski, Ö. Festin, P. Svedlindh, M. Haase, H. Weller, *JACS* **2003**, *125*, 9090–9101.
- [16] A. C. Johnston-Peck, J. Wang, J. B. Tracy, *ACS Nano* **2009**, *3*, 1077–1084.
- [17] a) K. Guo, H. Li, Z. Yu, *ACS Appl. Mater. Interfaces* **2018**, *10*, 517–525; b) J. Park, E. Kang, S. U. Son, H. M. Park, M. K. Lee, J. Kim, K. W. Kim, H. J. Noh, J. H. Park, C. J. Bae, J. G. Park, T. Hyeon, *Adv. Mater.* **2005**, *17*, 429–434.
- [18] F. Davar, Z. Fereshteh, M. Salavati-Niasari, *J. Alloys Compd.* **2009**, *476*, 797–801.
- [19] Y. Pan, R. Jia, J. Zhao, J. Liang, Y. Liu, C. Liu, *Appl. Surf. Sci.* **2014**, *316*, 276–285.
- [20] a) S. Carenco, C. Boissière, L. Nicole, C. Sanchez, P. Le Floch, N. Mézailles, *Chem. Mater.* **2010**, *22*, 1340–1349; b) M. Li, Y. Chen, N. Ji, D. Zeng, D.-L. Peng, *Mater. Chem. Phys.* **2014**, *147*, 604–610.
- [21] K. Mandel, F. Dillon, A. A. Koos, Z. Aslam, K. Jurkschat, F. Cullen, A. Crossley, H. Bishop, K. Moh, C. Cavelius, E. Arzt, N. Grobert, *Chem. Commun.* **2011**, *47*, 4108–4110.
- [22] B. D. Anderson, J. B. Tracy, *Nanoscale* **2014**, *6*, 12195–12216.
- [23] H. Loboué, C. Guillot-Deudon, A. F. Popa, A. Lafond, B. Rebours, C. Pichon, T. Cseri, G. Berhault, C. Geantet, *Catal. Today* **2008**, *130*, 63–68.
- [24] A. P. Grosvenor, M. C. Biesinger, R. S. C. Smart, N. S. McIntyre, *Surf. Sci.* **2006**, *600*, 1771–1779.
- [25] H. W. Nesbitt, D. Legrand, G. M. Bancroft, *Phys. Chem. Miner.* **2000**, *27*, 357–366.
- [26] a) P. E. R. Blanchard, A. P. Grosvenor, R. G. Cavell, A. Mar, *Chem. Mater.* **2008**, *20*, 7081–7088; b) S. Carenco, D. Portehault, C. Boissière, N. Mézailles, C. Sanchez, *Chem. Rev.* **2013**, *113*, 7981–8065.
- [27] S. Tougaard, *QUASES-IMFP-TPP2M Software*, Version 2.2., Physics Department, Odense University, Denmark, 2000–2002.
- [28] a) R. Arrigo, M. E. Schuster, S. Abate, S. Wrabetz, K. Amakawa, D. Teschner, M. Freni, G. Centi, S. Perathoner, M. Hävecker, R. Schlögl, *ChemSusChem* **2014**, *7*, 179–194; b) R. Arrigo, M. E. Schuster, S. Abate, G. Giorgianni, G. Centi, S. Perathoner, S. Wrabetz, V. Pfeifer, M. Antonietti, R. Schlögl, *ACS Catal.* **2016**, *6*, 6959–6966.
- [29] G. Akgul, F. A. Akgul, Y. Ufuktepe, *Vacuum* **2014**, *99*, 211–215.
- [30] G. van der Laan, J. Zaanen, G. A. Sawatzky, R. Karnatak, J. M. Esteve, *Phys. Rev. B* **1986**, *33*, 4253–4263.
- [31] S. E. Habas, F. G. Baddour, D. A. Ruddy, C. P. Nash, J. Wang, M. Pan, J. E. Hensley, J. A. Schaidle, *Chem. Mater.* **2015**, *27*, 7580–7592.
- [32] H.-R. Seo, K.-S. Cho, Y.-K. Lee, *Mat. Sci. Eng. B* **2011**, *176*, 132–140.
- [33] Y. Chen, C. Li, J. Zhou, S. Zhang, D. Rao, S. He, M. Wei, D. G. Evans, X. Duan, *ACS Catal.* **2015**, *5*, 5756–5765.
- [34] a) Tarachand, V. Sharma, J. Singh, C. Nayak, D. Bhattacharyya, N. Kaurav, S. N. Jha, G. S. Okram, *J. Phys. Chem. C* **2016**, *120*, 28354–28362; b) J. Singh, N. Kaurav, N. P. Lalla, G. S. Okram, *J. Mater. Chem. C* **2014**, *2*, 8918–8924.
- [35] J. Chen, Z. Duan, Z. Song, L. Zhu, Y. Zhou, Y. Xiang, D. Xia, *Appl. Surf. Sci.* **2017**, *425*, 448–460.
- [36] H. Winnischofer, T. C. R. Rocha, W. C. Nunes, L. M. Socolovsky, M. Knobel, D. Zanchet, *ACS Nano* **2008**, *2*, 1313–1319.
- [37] T. Ishizaki, K. Yatsugi, K. Akedo, *Nanomaterials* **2016**, *6*.
- [38] a) M. F. Sarac, R. M. Wilson, A. C. Johnston-Peck, J. Wang, R. Pearce, K. L. Klein, A. V. Melechko, J. B. Tracy, *ACS Appl. Mater. Interfaces* **2011**, *3*, 936–940; b) C. de Mello Donegá, P. Liljeroth, D. Vanmaekelbergh, *Small* **2005**, *1*, 1152–1162.
- [39] V. Humblot, S. Haq, C. Muryn, W. A. Hofer, R. Raval, *JACS* **2002**, *124*, 503–510.
- [40] A. Coelho, *J. Appl. Crystallogr.* **2018**, *51*, 210–218.
- [41] a) D. Balzar, in *Defect and Microstructure Analysis from Diffraction* (Eds.: R. L. Snyder, H. J. Bunge, J. Fiala), International Union of Crystallography, New York, **1999**; b) TOPAS Technical Reference, <http://www.topas-academic.net/>
- [42] A. Dent, G. Cibir, S. Ramos, A. Smith, S. Scott, L. Varandas, M. Pearson, N. Krumpa, C. Jones, P. Robbins, *J. Phys. Conf. Ser.* **2009**, *190*, 012039.
- [43] B. Ravel, M. Newville, *J. Synchrotron Radiat.* **2005**, *12*, 537–541.

 Manuscript received: October 16, 2019

Revised manuscript received: November 25, 2019

Accepted manuscript online: December 11, 2019

Version of record online: January 14, 2020